Nanostructured Copper Oxides and Phosphates from a New Solid-State Route

C. Díaz[1*], M .L. Valenzuela[2], V. Lavayen[3], K. Mendoza[1], D. O. Peña[4], and C. O'Dwyer[4*]

[1] *Departamento de Quimica, Facultad de Ciencias, Universidad de Chile, Casilla 653 Santiago, Chile*
[2] *Departamento de Ciencias Químicas, Facultad de Ciencias Exactas, Universidad Andres Bello, Av. Republica 275, 8370146, Santiago, Chile*
[3] *Faculdade de Química, Pontifícia Universidade Católica do Rio Grande do Sul, Porto Alegre - RS CEP 90619-900, Brazil*
[4] *Sciences Chimiques de Rennes, UMR-CNRS 6226, Université de Rennes 1, 35042 Rennes cedex, France*
[5] *Department of Physics and Energy, and Materials and Surface Science Institute, University of Limerick, Limerick, Ireland*

Abstract

Nanostructured copper containing materials of CuO, $Cu_3(PO_4)_3$ and $Cu_2P_2O_7$ have been prepared by solid-state pyrolysis of molecular $CuCl_2{\cdot}NC_5H_4OH$ (I), $CuCl_2{\cdot}CNCH_2C_6H_4OH$ (II), oligomeric $[Cu(PPh_3)Cl]_4$ (III), $N_3P_3[OC_6H_4CH_2CN{\cdot}CuCl]_6[PF_6]$, (IV) $N_3P_3[OC_6H_5]_5[OC_5H_4N{\cdot}Cu][PF_6]$ (V), polymeric chitosan$\cdot(CuCl_2)_n$ (VI) and polystyrene-co-4-vinylpyridine PS-*b*-4-PVP$\cdot(CuCl_2)$ (VII) precursors. The products strongly depend on the precursor used. The pyrolytic products from phosphorus-containing precursors (III), (IV) and (V) are Cu phosphates or pyrophosphates, while non-phosphorous-containing precursors (VI) and (VII), result in mainly CuO. The use of chitosan as a solid-state template/stabilizer induces the formation of CuO and Cu_2O nanoparticles. Copper pyrophosphate ($Cu_2P_2O_7$) deposited on Si using (IV) as the precursor exhibits single-crystal dots of average diameter 100 nm and heights equivalent to twice the unit cell *b*-axis (1.5 – 1.7 nm) and an areal density of 5.1 – 7.7 Gigadots/in^2. $Cu_2P_2O_7$ deposited from precursor (VI) exhibits unique labyrinthine high surface area deposits. The morphology of CuO deposited on Si from pyrolysis of (VI) depends on the polymer/Cu meta ratio. Magnetic measurements performed using SQUID on CuO nanoparticle networks suggest superparamagnetic behavior. The results give insights into compositional, shape and morphological control of the as-formed nanostructures through the structure of the precursors.

*To whom correspondence should be addressed:
E-mail: cdiaz@uchile.cl, Tel: +56 2 9787367, Fax: +56 2 2713888.
E-mail: colm.odwyer@ul.ie.

Introduction

In general, nanostructured materials can be prepared via two non-gas or vapor phase approaches: in solution or in a solid-state phase [1-3]. The most widely-known examples are in solution [4] but some solid-state [5-8] approaches have also been reported. Indeed, solution methods offer many advantages over the solid-state method, such as convenient control of the size and morphology of the nanoparticles and the ability to monitor the growth mechanism by other techniques such as optical spectroscopy for example. The solid state method, however, can more easily be incorporated into solid-state applications. For copper-containing nanostructured materials, several methods including hydrothermal techniques and sol-gel approaches, among others, have been reported [4a]. The preparation method for nanostructured CuO has been recently revised by Anadan [4a] and by Kuo and Huang for Cu_2O [4b]. Methods using ionic salts in single-batch hydrothermal or solvothermal conditions are the most common routes to obtain both Cu_2O and CuO. Direct oxidation of copper is of course a typical route to these copper oxides.

Copper oxides are p-type semiconductors having a band gap in the range 1-2 eV with excellent photovoltaic, electrochemical, and catalytic properties [4,9]. The discovery of high-T_c superconductivity in cuprates triggered interest in oxide materials as possible progenitors of exotic magnetic phenomena. Subsequent research established the important role of the two-dimensional (2D) CuO planes concerning the magnetism and superconductivity of the cuprates. The exploration of nanostructured copper-based materials as building blocks towards multifunctional materials with technological applications requires, among others, their incorporation in a solid-state phase, usually as thin films [10]. Thus the preparation methods for nanostructured materials in their solid-state phase are of great importance. Specifically for copper oxides, solid-state preparation methods have been reported [6,7,10-16]. Xu *et al.* [7] prepared CuO nanocrystals by a one-step solid-state reaction of $CuCl_2 \cdot 2H_2O$ and NaOH, while Kawahashi and Shiho [6] obtained hollow spheres by calcination of a polymer-coated $Cu(NO_3)_2$ salt. A different approach involves the oxidation of solid Cu under air at 400 °C to give CuO nanorods [10]. Similarly large-scale synthesis of CuO nanowires has been reported by thermal evaporation of a copper foil under oxygen flow [11].

On the other hand, Jiang *et al.* [12] reported the preparation of CuO nanowires by heating copper substrates in air. Recently, using the classical wet method starting from a Cu(II) salt and NaOH, the control

of the morphology was achieved by a proper choice of the molar ratio of the reactants [13]. A different approach involving the spray-pyrolysis of Cu(II) salts, has been also reported [14]. Tunable forms of CuO such as doughnut-like microstructures, microplates and multilayer microspheres were obtained using a Cu(II)/ethylene glycol precursor and calcination at 400 °C [15]. CuO nanoparticles inside Al_2O_3 have been recently prepared by gelation of the respective Cu(II) and Al(III) salts [16].

Although several preparation methods for nanostructured copper oxides have been reported, there is a scarcity of knowledge surrounding the growth of copper phosphate compounds and their nanostructured forms. To the best of our knowledge, the only known report concerning nanostructured copper phosphate $Cu_3(PO_4)_2$, highlights a 3D dandelion and 2D nanowall morphology [17]. Indirect evidence of the formation of $Cu_3(PO_4)_2$ and $Cu_5(PO_4)_3OH$ in soils was also recently reported [18].

In view of the scarcity of solid-state approaches to form nanostructured copper oxides and due to their importance of copper oxides and phosphates in lithium-ion batteries for example, we have been exploring new synthetic approaches for these phases. We report here a solid-sate method to form nanostructured copper-containing materials by a new approach using molecular, oligomeric as well as macromolecular precursors. These precursors are depicted in Scheme 1 and will be denoted throughout the paper as precursors (I) – (VII). As we previously reported, the use of metallic derivatives of phosphazenes as precursors leads to the formation of phosphorus-containing nanoparticles of phosphates or pyrophosphates [19-26]. With the aim of designing an alternative method to obtain nanostructured materials of metal oxides without using phosphorus, we show that this is possible using precursors I, II, VI and VII (see Scheme 1).

Chitosan and Poly(styrene-co-4vinylpyridine), PS-*b*-4-PVP, have been chosen as a macromolecular template/stabilizer because (a) they provide oxygen coordination sites (chitosan) as well as nitrogen and pyridine (PS-*b*-4-PVP), (b) they are inexpensive and commercially available polymers, and (c) chitosan can produced in large scale. Chitosan [27,28] is a polysaccharide obtained by deacetylation of natural chitin, which is one of the important natural polymers found in the shells of crustaceans and the cell walls of many fungi. Due to its oxygen linkages to nitrogen from the NH_2 groups and OH moieties present in the polysaccharide chains, it can bind metal ions forming macromolecular metal complexes [29]. Chitosan itself

can act as solution template/stabilizer for the formation of nanoparticles [29-31]. Here we show that chitosan can be successfully employed as solid-state template/stabilizer.

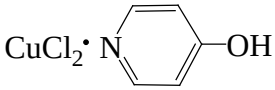

(I)

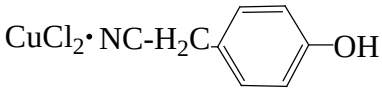

(II)

$[Cu(PPh_3)Cl]_4$

(III)

$[N_3P_3(OC_6H_4CH_2CN{\cdot}Cu)_6][PF_6]_6$

(IV)

$[N_3P_3(OC_6H_5)_5(OC_5H_4N{\cdot}CuCl)][PF_6]$

(V)

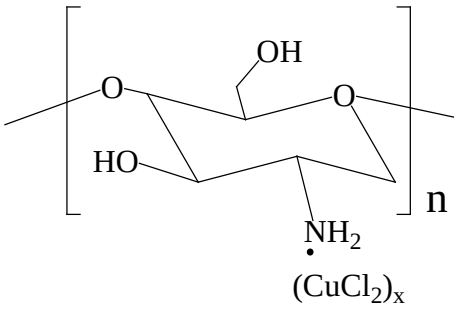

(VI)

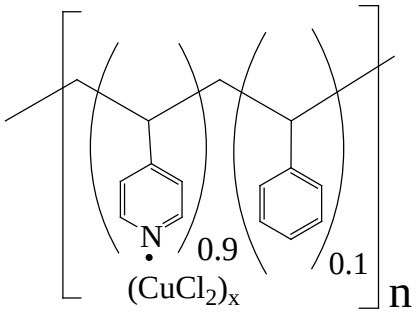

(VII)

Scheme 1. Formulae of precursors (I) – (VII).

On the other hand, poly(styrene-co-4vinylpyridine) is an interesting copolymer due to the vinylpyridine block which binds metal ions and the styrene groups which form shells, leading to stable macromolecular complexes [32-35]. PS-*b*-4-PVP has been used in solution as a template/stabilizer of metals and other nanoparticles [36-39], but no report has appeared concerning its use as solid-state template/stabilizer of nanoparticles. We report here, for the first time, the use PS-*b*-4-PVP as a solid-state template/stabilizer for copper containing nanoparticles. For all the precursors used (I)-(VII), the pyrolysis from (IV) resulted in the highest purity CuO and superparamagnetic properties determined by SQUID were also found.

Experimental Section

Preparation of Precursors

$CuCl_2 \cdot NC_5H_4OH$

$CuCl_2 \cdot 2H_2O$, 0.5 g, 2.94 mmol in 25 ml acetone and 4–hydroxipyridine, 0.28 g, 2.94 mmol in dichlomethane were stirred for 1 day. The green solution was concentrated to 5 ml and diethylether was added to give a brown solid. The supernatant was extracted and the solid washed with diethylether and dried under vacuum. Yield. IR (KBr, cm^{-1}): ν(OH): 3286; py coordinate: 1617; 1587; 1448; 1376; 1319; 1293; 1204; 1059; 1031 841; 828; 609; 528. Anal: Calc.(found): C 26.15(25.58); H 2.17(2.25); N 6.10(6.99).

$CuCl_2 \cdot CNCH_2C_6H_4OH$

$CuCl_2 \cdot 2H_2O$, 0.5 g, 2.94 mmol in 25 ml acetone and 4–hydroxibencylcyanide, 0.39 g, 2.93 mmol in dichlomethane were stirred for 1 day. The green solution was concentrated to 5 ml and diethylether was added to give a brown solid. The supernatant was extracted and the solid washed with diethylether and dried under vacuum. Yield IR(KBr, cm^{-1}): ν(OH): 3256; py coordinate: 1617; ν(CN): 2298; 1614; 1516; 1442; 1394; 1351; 1254; 1217; 1099; 1019; 841; 947; 901; 846; 808; 770; 643; 611. Anal: Calc.(found): C 35.89(36.06); H 2.61(3.4); N 5.23(5.15).

$N_3P_3[OC_6H_5]_5\,[OC_5H_4N \cdot Cu]\,[PF_6]$

Over $\{N_3P_3[OC_6H_5]_5[OC_5H_4N]\}$ 0.32 g, 0.61 mmol, 0.0785 g, 0.461 mmol of $CuCl_2 \cdot 2H_2O$ in 20 ml of methanol was added to NH_4PF_6, 0.1193g, 0.73 mmol and the solution stirred for 24h at room temperature. The solution was dried under reduced pressure and the solid residue extracted with dichloromethane. The solution was concentrated to a 5 ml volume and then diethylether was added. The precipitate was dried under vacuum to give 0.2 g. Yield: 48%. Anal: Calc.(found); C 46.53(46.8); H 3.21(3.2); N 6.20(4.09). ^{1}H NMR ($CDCl_3$, ppm.) 7.13 m; 6.89 m. ^{31}P NMR ($CDCl_3$, ppm) 8.43 singlet, (N_3P_3); -144.19 heptuplet, PF_6. IR (KBr, cm^{-1}): 2968; 2938; 2880; 1591. py coordinate: 1508; 1474; 1386; 1350; 1321; 1269; 1243; ν(PN): 1178; 1164; 1109; 1070; 1035; 1009; 951; 931; 881; 838; 792; 557.

Chitosan·$(CuCl_2)_n$ 5:1 and 10:1

Chitosan, 1.635 g, 9.43 mmol; 2.94 g, 16.84 mmol and $CuCl_2·2H_2O$, 0.5g , 1.869 mmol; 0.45 g, 1.68 mmol, molar relationships of 5:1; 10:1, respectively, were stirred in CH_2Cl_2 at room temperature for 6 days. The supernatant solvent was extracted with a syringe by decantation and the green solid washed with dichloromethane and then dried under reduced pressure. IR (KBr, cm^{-1}): ν(OH), ν(NH): 3422 (broad); 3280 (shoulder); 2924; 1686 (broad); 1321 ; 1116; 1018; 862; IR spectra for 1:5 and 1:10 products are similar.

PSP-PVP·$(CuCl_2)_n$

PVP and $CuCl_2·2H_2O$ in a molar relationship of 5:1 and 10:1 were stirred in CH_2Cl_2 at room temperature for 6 days. The supernatant solvent was extracted with a syringe by decantation and the green solid washed with dichloromethane and then dried under reduced pressure. The solids were insoluble in common organic solvents. IR (KBr, cm^{-1}): 3441; 2922; py coordinate: 1615; 1559; 1500; 1451; 1427; 1223; 1068; 1028; 831; 764; 706; 560. IR spectra for 1:5 and 1:10 products are similar.

The ligand $N_3P_3[OC_6H_5]_5[OC_5H_4N]$ [22] and its complex $[N_3P_3[OC_6H_5]_5[OC_5H_4N]·Cu][PF_6]$ [22] were prepared as reported previously. $[CuCl(PPh_3)]_4$ [40] and $N_3P_3[OC_6H_4CH_2CN·CuCl]_6[PF_6]_6$ [41] were prepared using literature methods. $CuCl_2·2H_2O$, NC_5H_4OH, $CNCH_2C_6H_4OH$, chitosan, NH_4PF_6 and PSP-PVP were purchased from Aldrich and used as received. The purity of chitosan was verified by IR as well as TG/DSC analysis. The solid was insoluble in common organic solvents.

Characterization

Infra-red (IR) spectra were recorded on an FT-IR Perkin-Elmer Spectrum BX II spectrophotometer. X-ray diffraction (XRD) was carried out at room temperature on a Siemens D-5000 diffractometer with θ-2θ geometry. The XRD data was collected using Cu-Kα radiation (40 kV and 30 mA). Scanning electron microscopy (SEM) and energy dispersive X-ray analysis (EDX) were acquired with a JEOL 5410 SEM with a NORAN Instrument micro-probe transmission microscope and with a JEOL JSM 6500F FESEM. Transmission electron microscopy (TEM) and electron diffraction were obtained using a JEOL JEM 1200

EXII microscope internally calibrated with a gold standard (Merck, 99.99% of purity; 85 kV, K = 4.1614 cm Å). The finely powered samples were dispersed in *n*-hexane and dropped on a conventional carbon-wasted copper grid. The diffraction patterns were obtained using a limiting field aperture of 20 μm. In this way, the diffraction from the grid is avoided and the observed area is minimized. The pyrolysis experiments were carried out, as previously reported [19-26], by pouring a weighed portion (0.05–0.15 g) of the solid on aluminum oxide boats placed in a furnace (Lindberg/Blue Oven model STF55346C-1) under a flow of air, heated from 25 to 300 °C and then to 800 °C, and annealed for 2 h. Raman spectra (using a 50 × objective) were recorded with a Renishaw Raman Microscope System RM1000 equipped with a 514.5 nm (2.41 eV) laser line. Output laser power was in the range 0.1–2.0 mW to avoid sample heating, unless otherwise specified. Atomic force microscopy (AFM) measurements were performed on a using a Veeco Enviroscope. Samples were prepared as previously reported [42] and dropped onto Si and oxidized Si (400 nm SiO_2) surfaces. Topological information was supplemented by lateral force and phase modulation imaging, respectively, to determine adhesion force changes and composition differences in the surfaces examined. Soft Si_3N_4-tipped cantilevers with a spring constant of 0.12 nN nm^{-1} were used in contact mode. Magnetic properties were acquired using a superconducting quantum interference device (SQUID) MPMS-XL5 magnetometer from Quantum Design, as a function of applied field and temperature down to 2 K.

Results and Discussion

Preparation and characterization of the precursors

Preparation of precursor I and II

As previously informed, these compounds were prepared by single coordination reactions of $CuCl_2$ with the respective ligands in ethanolic solution [41]. The products were characterized by standard spectroscopic as well as analytic methods (see experimental section). The IR spectra exhibits the typical bands of their coordinated ligands, *i.e.* ν[NC_4H_5], 1617 cm^{-1} for (I) and ν[CN], 2298 cm^{-1} for (II). The ν[OH] bands were observed at 3257 cm^{-1} and 3286 cm^{-1} for (I) and (II), respectively. Due to their paramagnetic character, NMR characterization was not possible for these precursors.

Characterization of precursors III, IV and V

The complex $[Cu(PPh_3)Cl]_4$ (precursor III) was prepared using methods reported in the literature [40]. The phosphazene $N_3P_3[OC_6H_4CH_2CN{\cdot}CuCl]_6[PF_6]_6$ (precursor IV) was prepared as previously reported [41]. $N_3P_3[OC_6H_5]_5[OC_5H_4N{\cdot}Cu][PF_6]$ (precursor V) was prepared as described in the experimental section. Characterization was achieved by usual spectroscopic as well as by elemental analysis. ^{1}H NMR spectrum exhibits the expected aromatic signal of both the phenyl as well as the pyridine groups. On the other hand, the ^{31}P NMR spectrum clearly shows the signal of the phosphazene ring at 8.43 ppm as well as the typical heptuplet signal of the PF_6 anion at -144.19 ppm. The IR spectrum exhibits the characteristic band at 1617 cm^{-1} of coordinate pyridine. As previously reported for $N_3P_3[OC_6H_5]_5[OC_6H_4CH_2CN{\cdot}Cu][PF_6]$, the complex exhibits the characteristic white color of the paramagnetic Cu(I) compounds [41]. It is interesting to note that attempts to prepare other copper derivatives with cyclotriphosphazenes were unsuccessful.

Characterization of precursors VI and VII

The chitosan$\cdot(CuCl_2)_n$ and the (PS-*b*-4-PVP)$\cdot(CuCl_2)_n$ precursors were prepared by a direct coordination reaction, in two initial Cu(II)/chitosan or Cu(II)/PS-*b*-4-PVP molar proportions: 1:5 and 1: 10. The two types of products contain different Cu content linked to the polymeric chain and related to the initial Cu content. Solid products exhibit the characteristic shift of IR spectral bands for both types of compounds: 3280 cm^{-1} for (VI) and typical pyridine ring vibration at 1615 cm^{-1} for (VII). The broad ν(OH) in chitosan [28] becomes unfolded upon coordination, appearing a new band around 3100 cm^{-1}. On the other hand, for pyridine coordination, a new band centered at 1600 cm^{-1} emerges [22].

Additionally, the thermogravimetric (TG) curves exhibit the typical weight loss corresponding to the carbonization of the organic matter at 400 °C for VI and VII. Consistently with this, both DSC curves show an exothermic peak at ~410 °C typical of the carbonization of the organic residues.

Binding properties of chitosan with metal ions are well known: metal ions can bind to chitosan, probably via electrostatic interactions, to oxygen or nitrogen atoms depending on the properties of the metal ion. In non-polar media such as dichloromethane, the resulting macromolecular metal-complex might be

insoluble and eventually precipitates. In that case, a macromolecular metal complex having a regular distribution of metal centers through a chain could be a suitable template for the solid-state formation of nanoparticles after elimination/combustion of the organic matter.

Pyrolysis of the precursors

As previously mentioned, the pyrolysis of the precursors I–VII were performed at 800 °C in air [19-23]. Pyrolysis of precursors I and II result in CuO, as evidenced by their powder XRD patterns. Figure 1a shows the XRD spectrum for precursor (II). EDAX analyses of the products in Fig. 1b, indicates the presence of copper and oxygen as the main elements. The SEM image in Fig. 1c, shows an irregular morphology comprising particles are various sizes. Consistently, TEM analysis, shown in Fig. 1d, shows the presence of large agglomerates of structures.

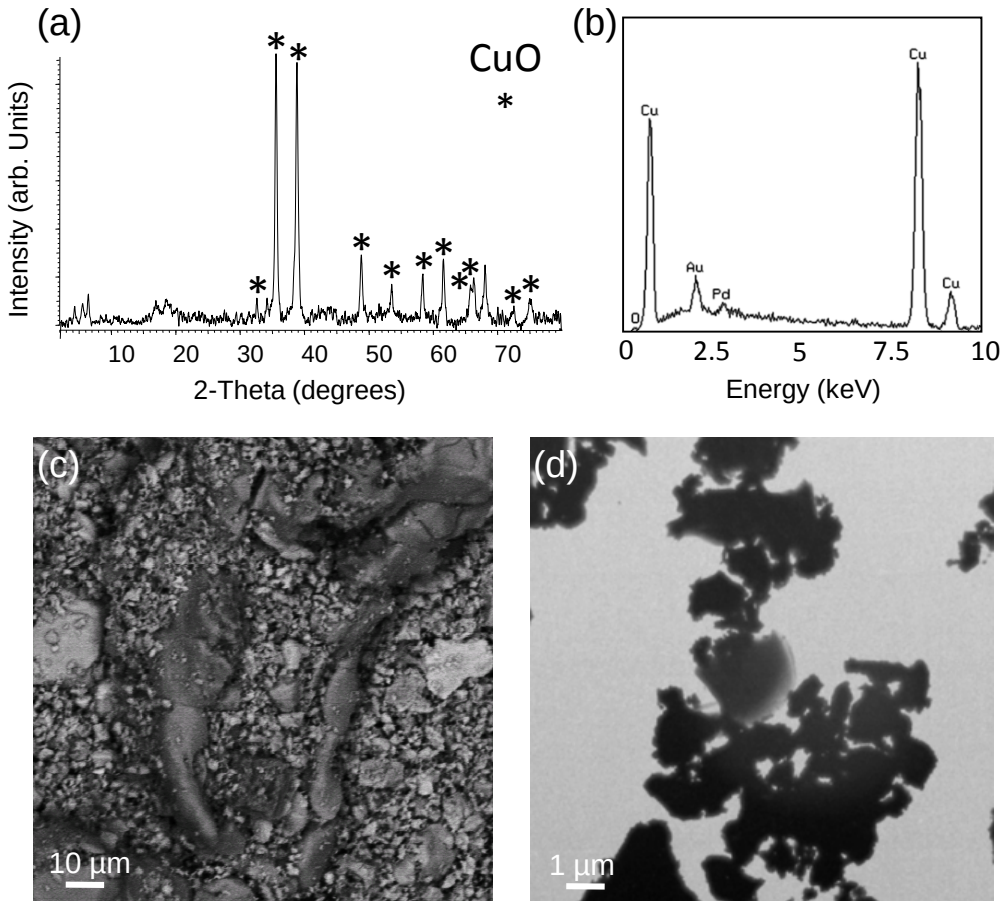

Fig. 1 (a) XRD spectrum of the pyrolytic product from precursor (II) indexed to monoclinic CuO (tenorite), Space Group C/2c. (b) Corresponding EDAX profile and (c), SEM and (d) TEM image of product morphology.

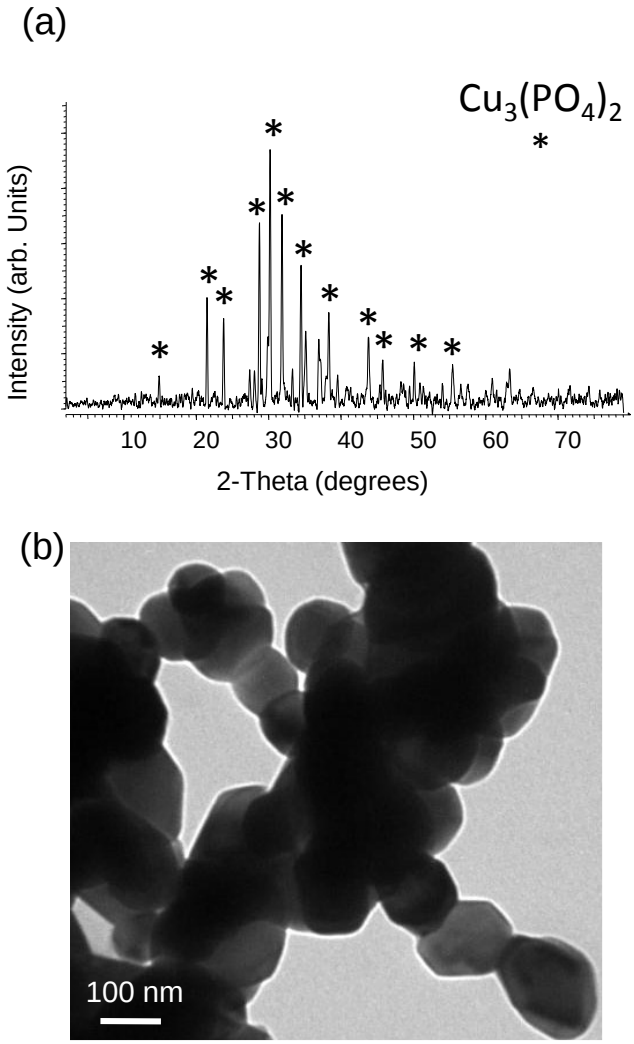

Figure 2. (a) XRD spectrum of the pyrolytic product from precursor (III). The main intensity peaks from the theoretical pattern for $Cu_3(PO_4)_3$ are highlighted (JCPDS 70-0494); all peaks match the single crystal standard pattern. (b) TEM image of product morphology showing a fused grain structure for smaller crystals.

Pyrolysis of the oligomeric complex $[Cu(PPh_3)Cl]_4$ (precursor III)] results in nanostructured $Cu_3(PO_4)_3$ (Fig. 2a) consisting of particles joined together in a characteristic fused-grain morphology with each particle typically ~200 nm in size, as shown in the TEM image in Fig. 2b. EDAX analyses (not shown) evidence the presence of Cu, P and O.

On the other hand, pyrolysis of precursors IV and V results in the formation of $Cu_2P_2O_7$ in both cases. XRD analysis confirms this uniphasic crystal structure (Fig. 3a) indexed to monoclinic $Cu_2P_2O_7$, Space Group C2/c. The morphology is found to be dependent on the precursor used; the typical porous network morphology is seen in Fig. 3b. EDAX analyses (not shown) evidence the presence of Cu, P and O only. The TEM images exhibit somewhat large agglomerate nanostructures as shown in Fig. 3c which constitute the larger networked agglomerates of the overall product.

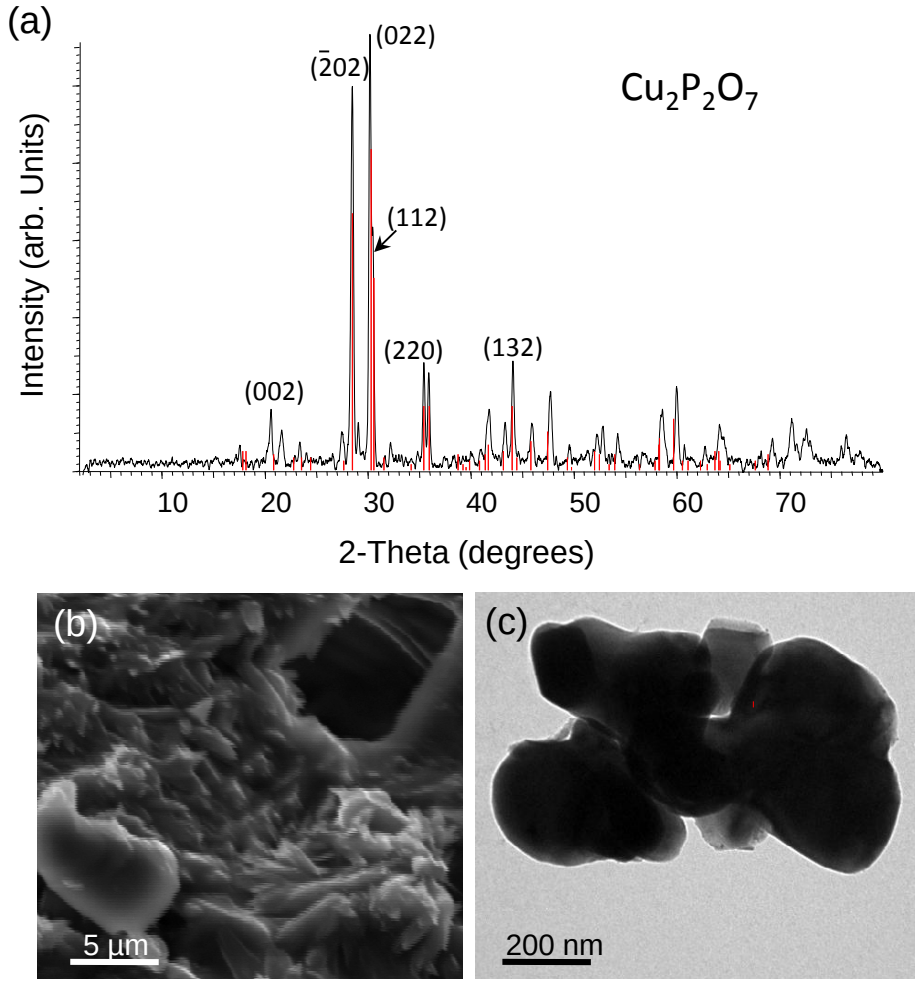

Figure 3. (a) XRD spectrum of the pyrolytic product from precursor (III). The red lines are the theoretical pattern for $Cu_2P_2O_7$. (b) SEM and (c) TEM image of product morphology showing an agglomerated granular morphology.

Pyrolysis of the macromolecular precursors VI and VII give in both cases, almost pure CuO, as evidenced by their XRD spectra shown in Fig. 4a. However, closer inspection of the diffraction spectrum from the pyrolyzed precursor VI (see Fig. 4b) also shows the presence of Cu_2O and traces of $Cu(OH)_2$. The approximate composition of these phases is determined to be: Cu_2O (10-15%), $Cu(OH)_2$ (2%), CuO (81-87%) using quantitative EDX analysis coupled to the Reference Intensity Ratios (RIR) methodology from XRD, where only the strongest diffraction intensities of the phases observed in the X-ray pattern (see supporting information Fig. S1). Estimates were also made of the size of the CuO nanoparticles using the Scherrer formula using the CuO (111) diffraction peak [44]. Assuming a homogeneous strain across the crystallites, the size of the grains can be estimated from the full-width half-maximum (FWHM) values of the diffraction peaks. From these values it can be seen that as-grown films exhibit characteristics of a

nanocrystalline structure with similar crystallite sizes; the crystallite sizes are estimated to be in the range 22–32 nm.

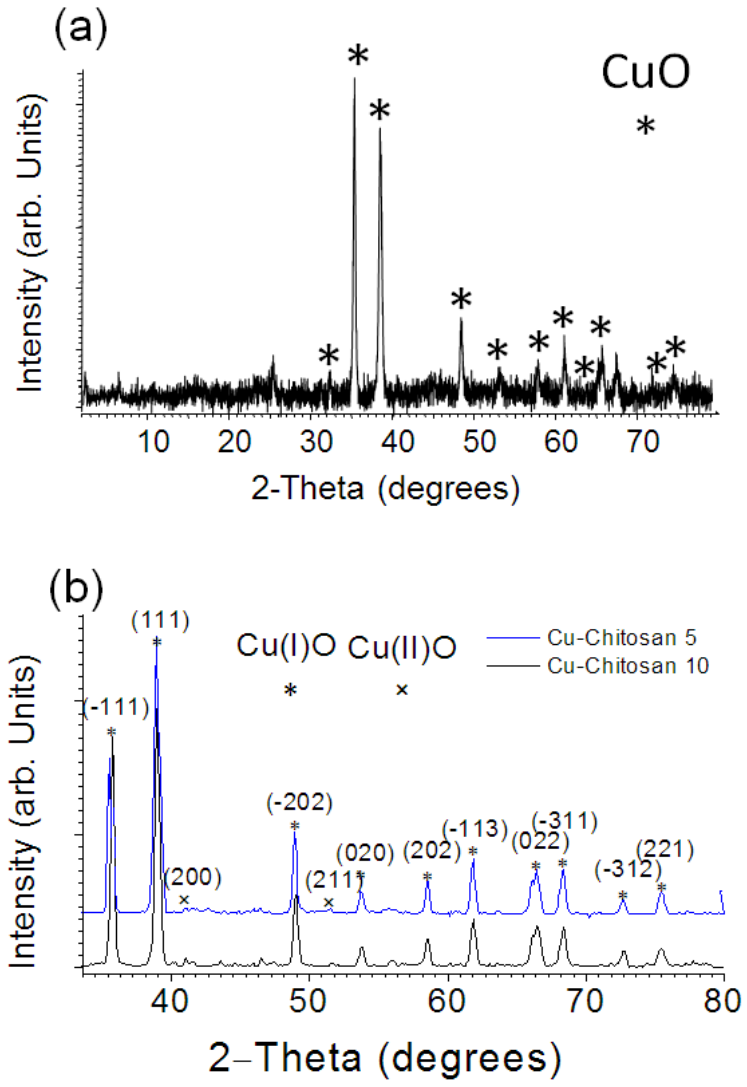

Figure 4. (a) XRD spectrum of the pyrolytic product from precursor (VI) and (VII). (b) XRD patterns showing detailing the presence of CuO and also some Cu_2O and $Cu(OH)_2$ phases in the product.

An investigation of the temperature dependence and the chitosan:$CuCl_2$ ratio was performed for precursor VI. Pyrolysis at two temperatures (600°C and 800 °C) and at two chitosan:$CuCl_2$ ratios (10:1 and 5:1) were investigated. Different morphologies were observed for the two chitosan:$CuCl_2$ ratio precursors, as seen from the bright and dark field SEM images in Figs. 5a and 5b. Some minor differences in the average particle size and morphology are found from TEM analysis, as shown in Figs 5c and 5d, where fused grain networks are characteristic from the 10:1 ratio mixture. Their corresponding electron diffractions patterns match those from XRD, confirming crystallite formation of these phases at the nanoscale.

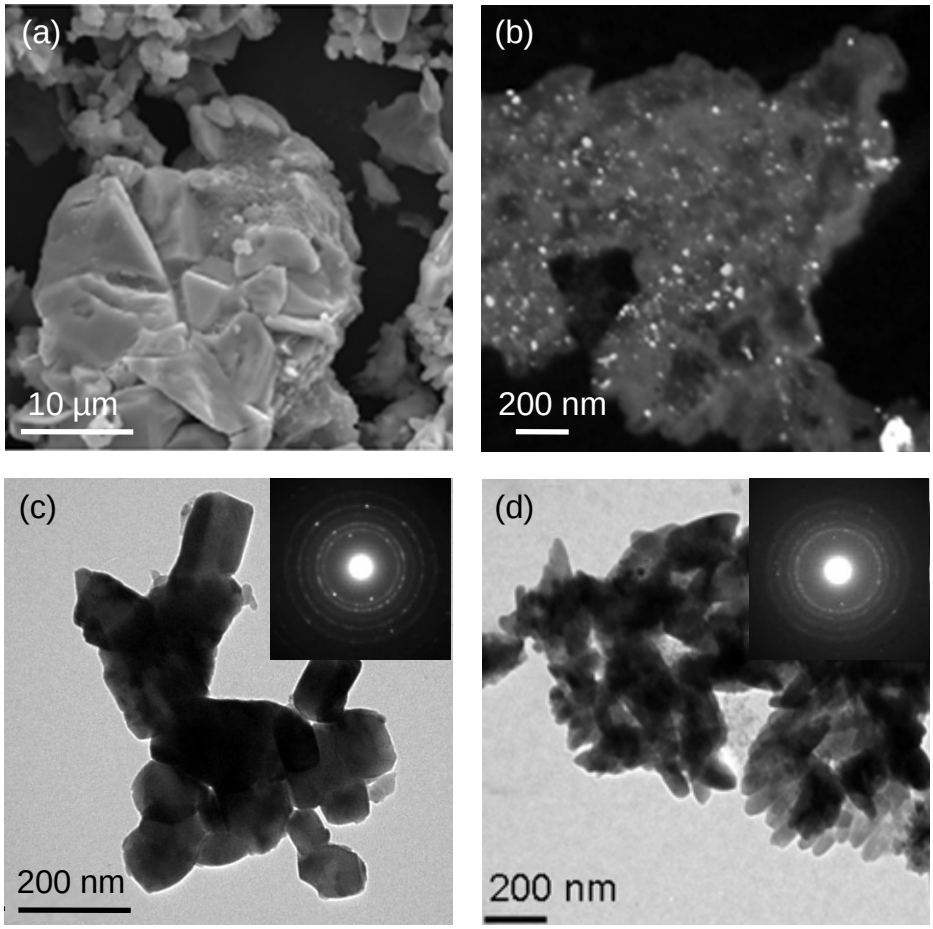

Figure 5. (a) SEM secondary electron image and (b) electron backscattered image of pyrolytic products from chitosan:$CuCl_2$ with ratios of 10:1 and 5:1, respectively. (c,d) Corresponding TEM images and associated electron diffraction patterns of the products shown in (a,b).

Different temperatures of pyrolysis did not produce alterations in neither the composition nor in the morphology. A detailed analysis of the TEM of this latter sample (see Fig. 6) shows the presence of quasi-circular nanoparticles with an average diameter of ~40 nm. A series of dark field TEM images from the pyrolytic product from copper oxide-chitosan in Figs 6b-d, were taken at a range of tilt angles between 15 and 30°. Electron diffraction spots show the presence of CuO and $Cu(OH)_2$ phases, corroborating the phase identification from X-ray analysis.

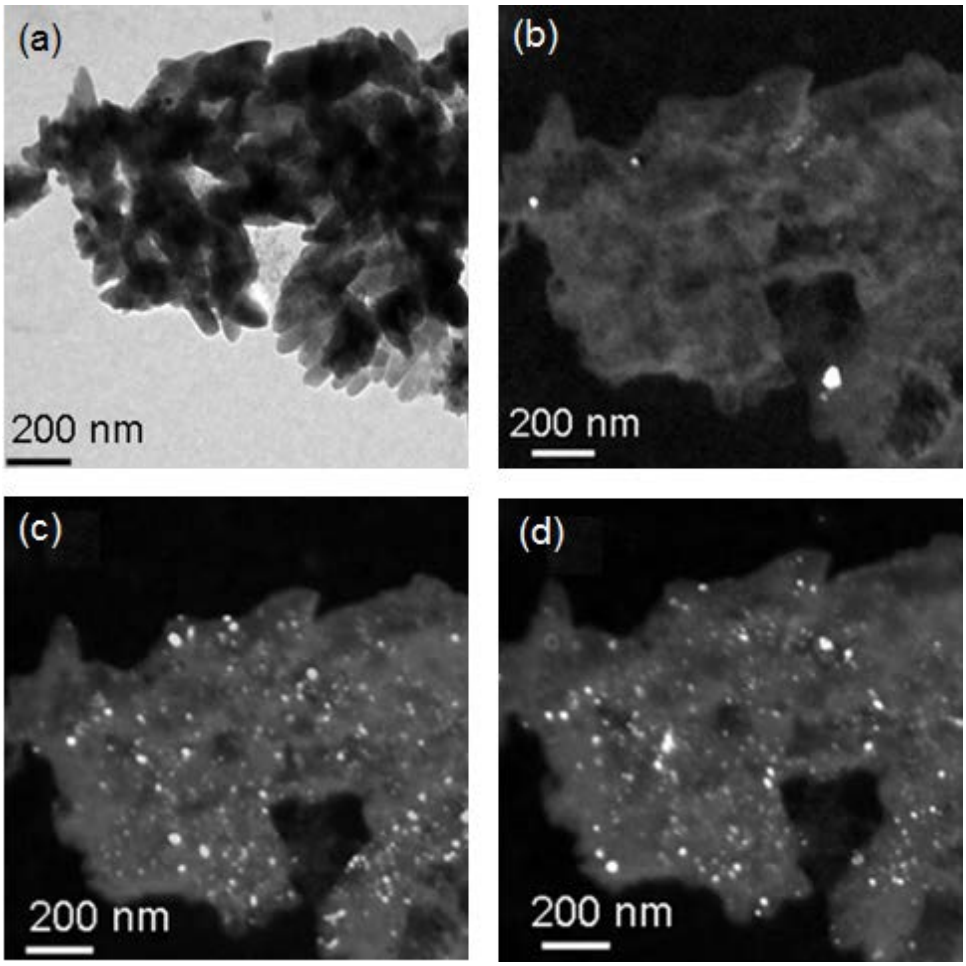

Figure 6. (a) Bright field TEM image of the nanostructured product from precursor (VI). (b-d) Dark field TEM image series where the sample is tilted between 15-30° highlighting CuO crystals (bright points) of various relative orientation.

Additional evidence of the presence of CuO and Cu_2O in precursor VI was obtained by Raman spectroscopy. As shown in Fig. 7a, the Raman spectrum of pyrolyzed precursors (1:10 ratio) shows the four Raman vibrational modes at 287 cm^{-1} (A_g), 353 cm^{-1} (B_g), 621 cm^{-1} and 1006 cm^{-1}, that are red-shifted with respect to the CuO bulk [45]; quantum confinement effects observed in CuO nanowires previously, have been linked to peak broadening [46].

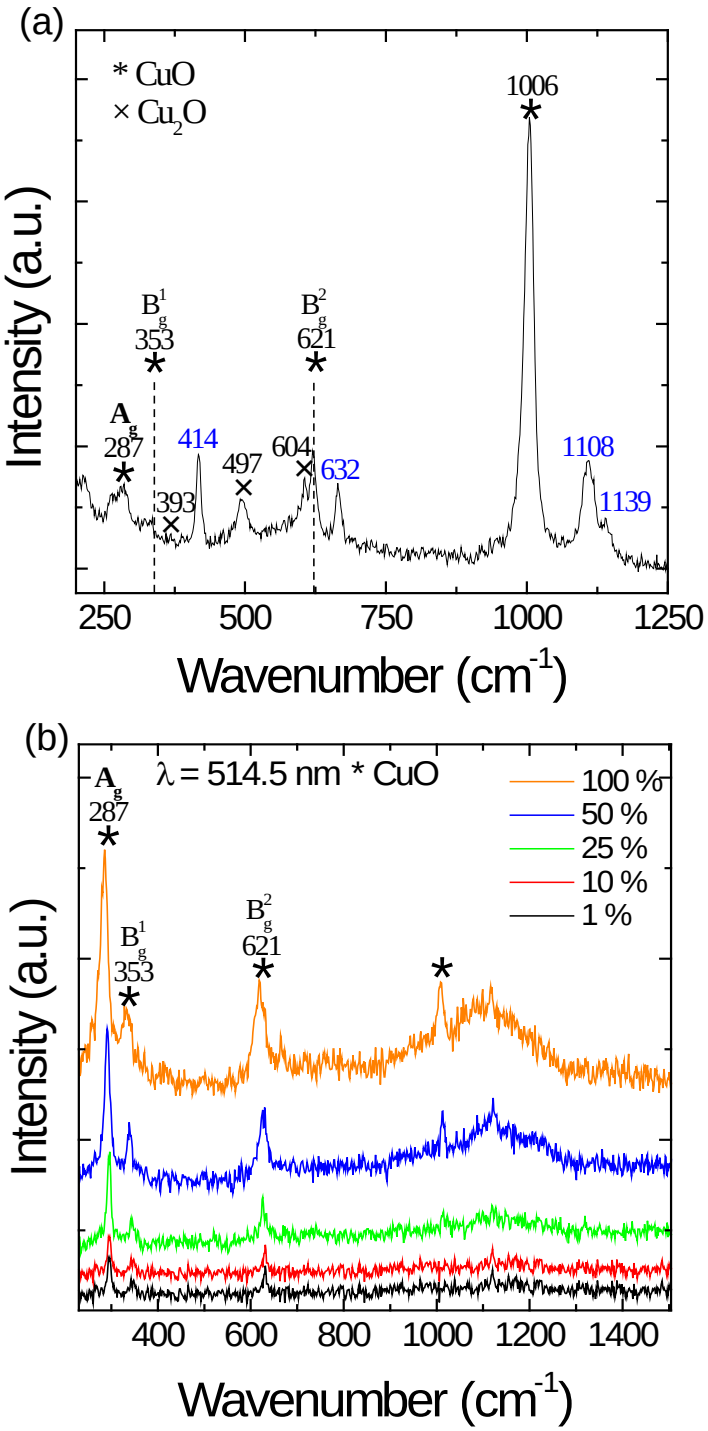

Figure 7. (a) Raman spectrum of the pyrolyzed copper oxide sample contain a ratio 1:10 Cu:chitosan. (b) Raman spectra of the pyrolyzed copper oxide sample contain a ratio 1:10/ Cu:chitosan as a function of laser power density.

Additionally, Raman spectra of the pyrolyzed products of the organic species in the copper oxide-chitosan samples reveal the formation of several remnant carbon clusters at metal surface. Indeed, Raman spectroscopy is an extremely sensitive tool for the detection of carbon clusters [47]. We do not observe any carbon related D and G bands in the spectra, indicating successful elimination of carbon contamination and

carbon-containing residue during the typical operating temperature range (see Experimental section) of a copper catalyst [48].

Raman shifts found at 287, 393, 497, and 604 cm^{-1} for the copper oxide pyrolyzed sample correspond to Raman active modes from Cu_2O. The low intensity band at 287 cm^{-1} indicates sub-stoichiometric Cu_2O [49]. The surface termination of the oxides was also assessed and the peaks at 1108 cm^{-1} and 1139 cm^{-1} can be assigned to the ν(C–O) stretching vibration of adsorbed methoxy (CH_3–O–) groups from the chitosan additive. On Cu (110) surfaces, the band assigned to the ν(C–O) stretching vibration from adsorbed methoxy groups was previously observed at 1014 and 1020 cm^{-1}, corroborating the findings for these pyrolytic products.

Figure 7b shows Raman spectra from the pyrolyzed copper oxide sample containing a Cu:chitosan ratio of 1:10, from precursor VI. Using a visible laser line (514.5 nm) with a different output beam power range (5 μW – 0.2 mW) to probe the CuO specifically rather than the organic additive, we observe the principle Raman active modes (A_g^1, B_g^1) from CuO varies. The spectra show that at a laser powder density of 66 mW cm^{-2}, localized Joule heating and burning processes occur, which account for the deconvoluted band between 1050-1200 cm^{-1} owing to the presence of organic matter bound to the CuO phase.

From the TEM image in Fig. 6a, rod-like structures of copper oxide containing many single crystallites embedded into a host matrix (organic) were visible; Fig. 8 shows such regions in more detail. The electron diffraction pattern (Fig. 8b) shows the presence of non-uniform and continuous rings from the CuO phase; similar characteristics were reported in cuprous oxide nanowires prepared by an additive-free polyol process [50]. The pattern was indexed to monoclinic CuO (Space Group: C/2c) and shows the presence of (002), (202), (-101), (-220), (022) reflections from CuO and some preferential texturing of the phase is observed related to the anisotropic growth. Similar findings have been previously found for branched CuO nanowires [51]. Stereographic analysis showed that the tips of the CuO rod-like crystals are faceted suggesting an influence of several orientation of the crystal with respect to the viewing zone axis.

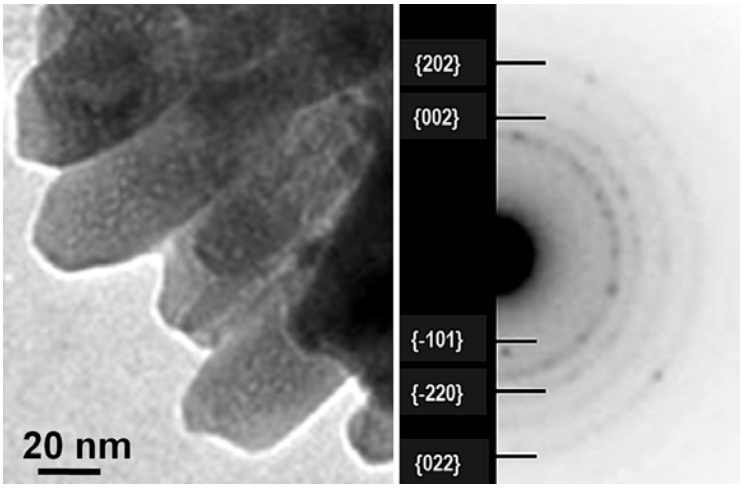

Fig. 8 TEM image of the quitosan-CuO-M_2 sample showing rod-like nanostructures and corresponding selected area electron diffraction spot along the [001] zone axis.

Table 1. Summary of some properties of pyrolytic products.
[a] Main product from XRD. [b] Morphology from SEM data. [c] Particle size from TEM data.

Precursor	**Product**[a]	**Morphology**[b]	**Particle size**[c]
$CuCl_2{\cdot}NC_5H_4OH$ (I)	CuO	Irregular (porous/dense)	Agglomerates
$CuCl_2{\cdot}CNCH_2C_6H_4OH$ (II)	CuO	Irregular (porous/dense)	Agglomerates
$[Cu(PPh_3)Cl]_4$ (III)	$Cu_3(PO_4)_3$	Fused grains	200 nm (avg.)
$N_3P_3[OC_6H_4CH_2CN{\cdot}CuCl]_6[PF_6]$ (IV)	$Cu_2P_2O_7$	3D-porous	Large nanoparticle agglomerates
$N_3P_3[OC_6H_5]_5[OC_5H_4N{\cdot}Cu][PF_6]$ (V)	$Cu_2P_2O_7$	3D-network/dots	Agglomerates/single crystals
Chitosan$\cdot(CuCl_2)_n$ (VI)	CuO	Dense fused platelets	Quasi-spherical particles
PS-*b*-4-PVP$\cdot(CuCl_2)$ (VII)	CuO	Foams	N/A

In comparison, the main difference in the CuO products obtained from pyrolysis of (VI) and (VII) are the resultant morphology. In contrast with the dense morphology observed for pyrolytic products from (VI), a high surface area foam morphology is found for the pyrolytic product from (VII) (see supporting information Fig. S2). A comparison of the resulting products is summarized in Table 1 for all precursors investigated.

Insights into the Formation Mechanism

From the pyrolysis of the precursors II, IV and V containing phosphorus atoms, it is clear that copper phosphates or pyrophosphates are present post-pyrolysis. This corroborates our previous results that pyrolysis of organometallic derivatives of cyclotriphosphazenes yields metallic nanostructured phosphates

or pyrophosphates [19-26]. The results from precursor II also corroborate this hypothesis even if no cyclophosphazenes are present since the phosphine acts as the source of phosphorus atoms.

Also, our results from precursors I, II and VI confirm the hypothesis that precursors that do not contain phosphorus, the product can either be a metallic oxide or simply a metal in cases where a noble metal center is coordinated to the macromolecular complex. Comparing the results obtained from precursors I and II with VI and VII, the TEM images show the formation of mainly small nanoparticles from VI and VII, due most probably to the stabilizer/template function of the PVP and chitosan polymers. On the other hand, it is well known that in solution, polymers are necessary as stabilizers or templates to give low diameter nanoparticles. It appears then that in the solid-state the presence of stabilizers or templates is also necessary to drive the formation of small and controllably-sized nanoparticles.

CuP_2O_7 and related pyrophosphates are not readily synthesized in crystalline form through synthetic routes in the solid-state. We have shown that such pyrophosphate phases form with intricate surface deposition patterns heavily related to the mechanism summarized above, *i.e.* labyrinthine, coral and fractal surface depositions which depends on the metal center and the mixture ratio. This is also the observation even when Cu is used as the metal center. The characteristic features of CuP_2O_7 are CuO_4 square sub-units which share four corner oxygens with two P_2O_7 diphosphate groups, forming a chain of corrugated ribbons of $[CuP_2O_7]_\infty$ along the *c*-direction. Here, only the pyrophosphate phase is observed to have a non-particle-like morphology.

Direct precursor deposition and pyrolysis on surfaces

Suitable samples for AFM observations of precursors IV and V, deposited on Si and SiO_2, were prepared using a previously reported methodology [42]. Figure 9 displays the AFM images of the main features of two pyrolytic products. The morphology depends on both the substrate and the nature of the precursor. For the as-deposited $Cu_2P_2O_7$ from precursor IV on Si, two sets of features and related sizes were observed: micron-scale large faceted single crystal islands (the largest being ~1 μm), as shown in Fig. 9a, and small islands of average height ~27 nm and ~60 nm in width, seen in Fig. 9b. On the other hand, for the same nanostructured material deposited on SiO_2, somewhat regular islands of $Cu_2P_2O_7$ were observed with

height of about 37 nm (not shown) and widths in the range 150 nm – 250 nm. Analysis of the particles size distributions for both deposits shows that the size distribution follows a power-law consistent with fractal size scaling, *i.e.* for each scanned area measured by AFM, the distribution of particles sizes is self-similar. This is found for deposits from precursors IV and V where individual particles result.

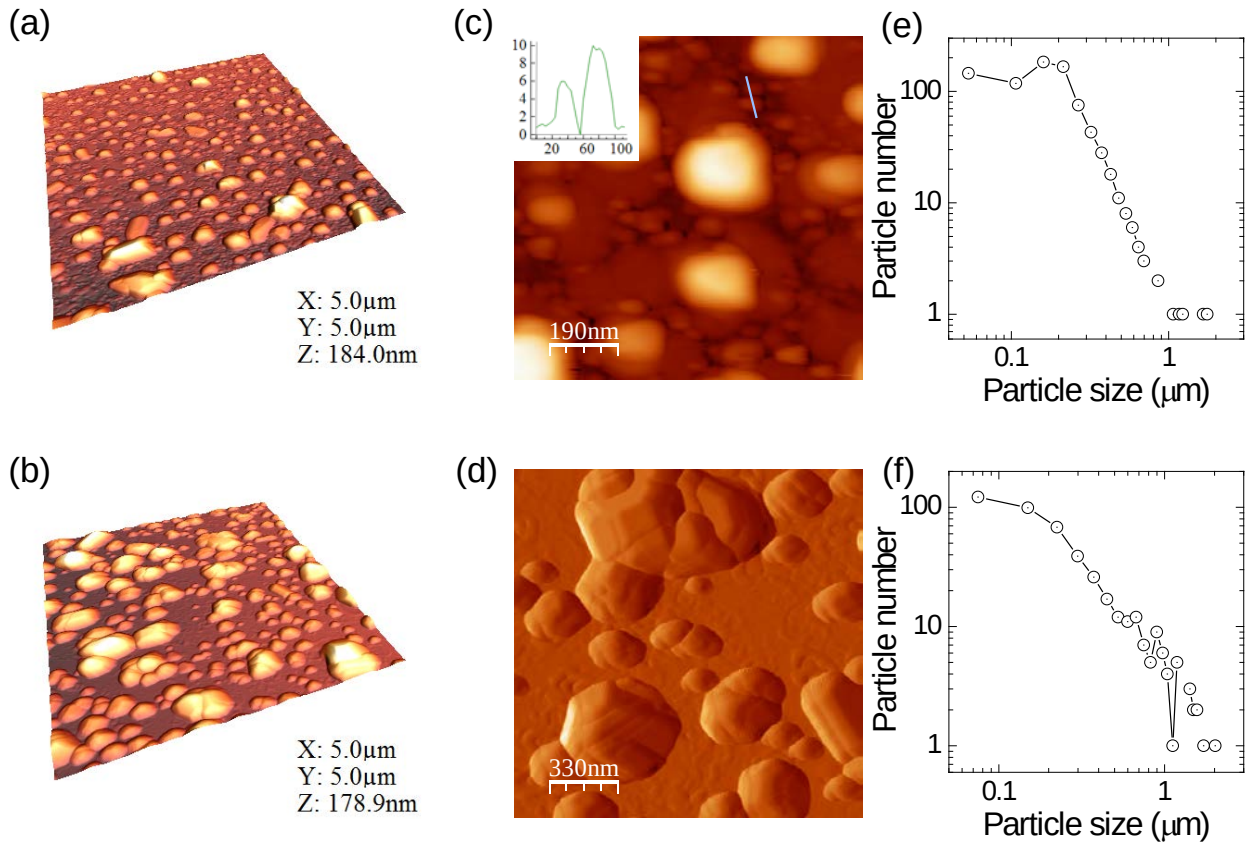

Figure 9. AFM images of the pyrolysis products from IV (a and b) and from V (c and d), showing the main features of surface deposited crystals. (e,f) Corresponding particle size distribution from (a) and (c).

The as-deposited $Cu_2P_2O_7$ from precursor V on Si exhibits two main shapes located in two different zones: a wavy/labyrinthine deposit seen in Fig. 10a, and small island structures (not shown). The former type have widths of ~60 nm and are typically ~700 nm in length, while the islands are in the micrometer size range (1-5 µm). Similar coral-like structures have been observed for SnP_2O_7 and are characterized by a self-affine fractal morphology with metallic clusters throughout each wavy feature [42]. The same precursor deposited on SiO_2 results in a granular deposit morphology comprising pseudo-spherical and pseudo-cubic cubic shaped nanostructures of various heights, as shown in Fig. 10b. The island-shaped CuP_2O_7 growths exhibited an average height between 1.5-1.7 nm, as evaluated from histogram analysis of surface profile for

many individual particles, taking background noise, tip deconvolution and roughness effects into account, with corresponding diameters of ~100 nm. Analysis of the vertical height of these extremely flat crystal deposits corresponds to roughly double the length of the unit cell *b*-axis, implying a surface deposition of CuP_2O_7 single crystal dots with self-similar surface orientation with respect to the substrate. Investigations of larger area deposits shows that these single crystal dots form with areal densities between 5.1 – 7.7 Gigadots/in^2.

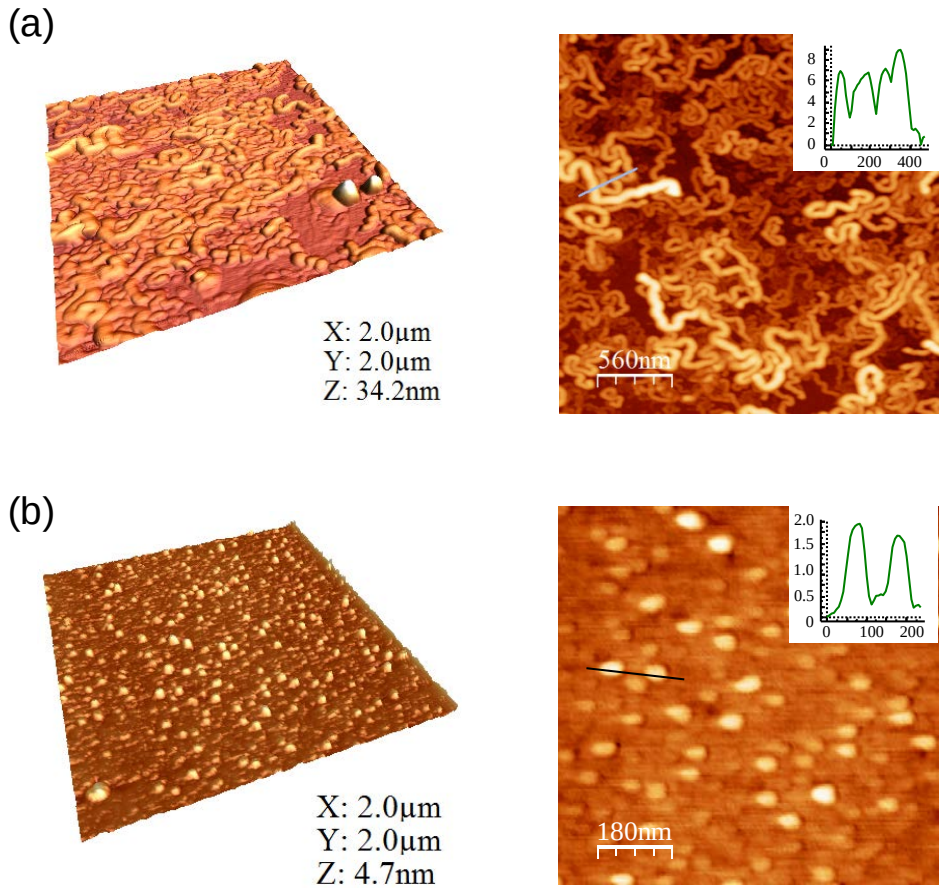

Fig. 10 AFM images of the surface deposited morphology of pyrolyzed products from precursor (V) showing networked and individual CuP_2O_7 nanostructures.

For precursor VI, where mainly CuO was obtained, AFM studies were also performed by depositing the copper oxide. For the CuO obtained from chitosan·$(CuCl_2)_n$ with a ratio of 5:1, a mixture of hillocks and triangular platelets were obtained. Examples of the typical shapes observed are shown in Fig. 11a, and all features have sub-micrometer lengths in all dimensions. In contrast, for the CuO deposited from the chitosan·$(CuCl_2)_n$ precursor with a ratio of 10:1, irregular hillocks of ~50 nm in height and 100-300 nm in

width were obtained (Fig. 11b). With chitosan polymers, the pyrolysis on surfaces shows only minor variations in the resulting morphologies and crystal sizes, where the amount of CuO deposited per unit area scales with the Cu concentration in the precursor, indicating and similar decomposition mechanism for both mixtures during pyrolysis.

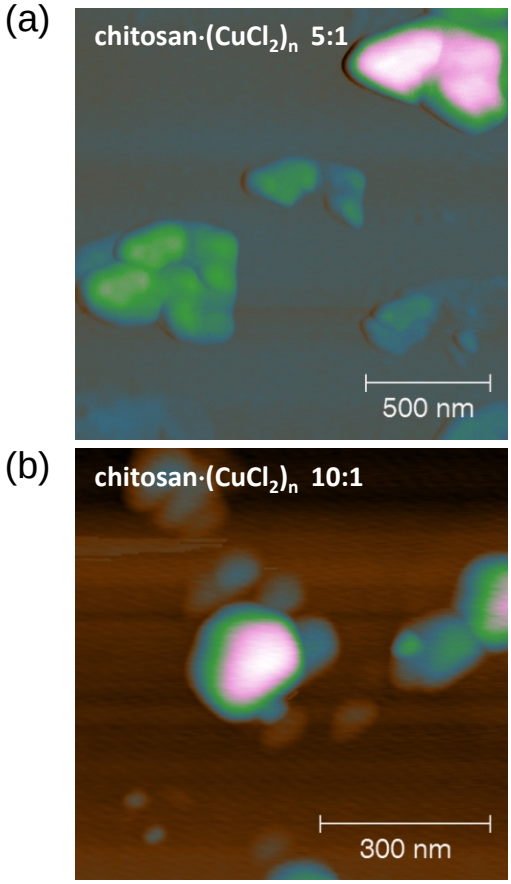

Fig. 11 AFM images of CuO deposited from precursor VI in the solid state as (a) chitosan·$(CuCl_2)_n$ 10:1 and (b) chitosan·$(CuCl_2)_n$ 5:1 mixtures.

Low Temperature Magnetic Measurements

Since precursor VI affords almost pure nanostructured CuO, we investigated the possibility that is displays magnetic interactions. Data shown in the main panel of Fig. 12 was taken after cooling the sample (23.9 mg) down to the lowest temperature (2 K) in a field of 500 Oe. The sample was then cooled in the presence of the same applied field (M^{FC}). A large irreversibility is observed between the zero-field-cooled (ZFC) and field-cooled (FC) processes, showing a non-equilibrium behavior and presence of magnetically ordered Cu(II) centers even at room temperature. The maximum observed in the ZFC curve is a clear

indication of the existence of a superparamagnetic state occurring in this material, composed of grains of nanoscale dimensions, as discussed above. This behavior is lost at temperatures greater than 280 K as indicated by the absence of FC/ZFC curve separation. The associated blocking temperature is found to be 230 K; such a high temperature indicates strong interaction between the nanoparticles, which are typically joined together as shown above. In order to confirm the magnetic order, we performed isothermal magnetization measurements M(H) at two characteristic temperatures (5 and 300 K), by varying the applied field between 0 and 50 kOe, shown in Fig. 12. A large hysteresis is obtained at 5 K, while minimal irreversibility is observed at room temperature, despite the fact that the sample is still in the magnetically ordered state. The measured saturation magnetization is found to be 0.13 emu/g at 5 K, but reduces to 0.07 emu/g at 300 K and the remanent magnetization of the nanoparticles is 0.06 emu/g at 5 K, but the nanomaterial retains 30% of its remnant magnetization at 300 K. These features are characteristic of a superparamagnetic behavior in nanosized materials.

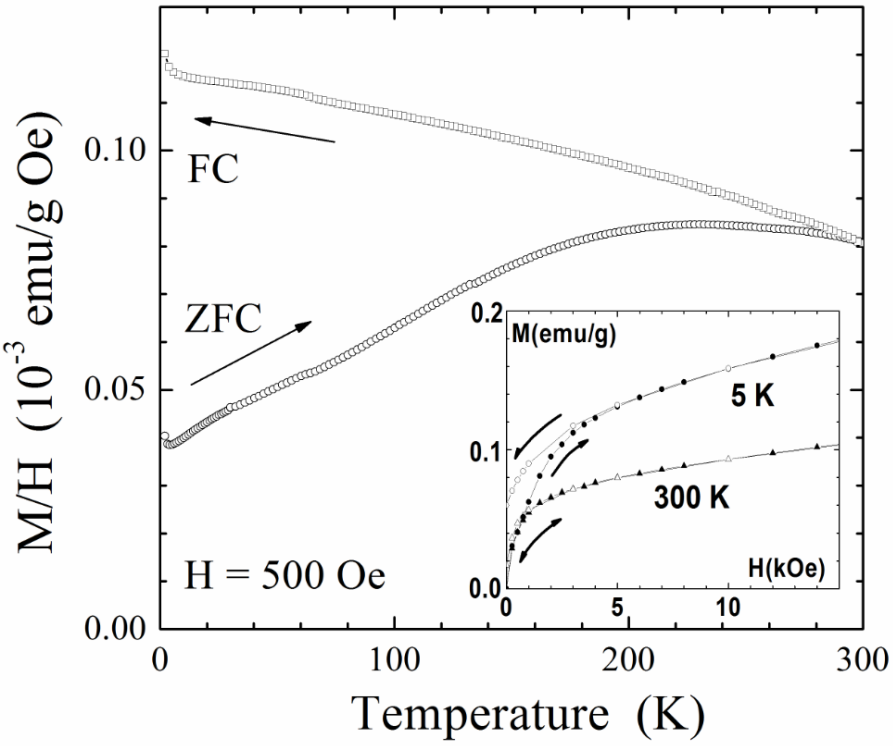

Fig. 12 Temperature (main panel) and field (insert) dependence of the magnetization for the pyrolytic product obtained from a chitosan·$(CuCl_2)_n$ precursor prepared in a molar ratio of 5:1.

The magnetic behavior of nanostructured CuO *i.e.* ferromagnetic response, has been explained by uncompensated surface spins, particle size effects and cation/anion vacancies [52-55], however the true

origin of this behavior is still a matter of investigation, due most likely to the complicated surface effects including oxygen vacancies and a mixture of +1 and +2 valence states. These explanations could be interlinked due to a higher density cation/anion vacancy distribution on surfaces of nanoparticulate assemblies and agglomerates, much greater than would be found in an equivalent bulk mass.

Conclusions

We have investigated the synthesis and use of several molecular, oligomeric and macromolecular complex derivatives of CuCl and $CuCl_2$ as solid-state precursors of nanostructured copper oxides and phosphate nanomaterials such as single crystal CuO, $Cu_3(PO_4)_3$ and $Cu_2P_2O_7$. The composition, and morphology of the pyrolytic products were significantly affected by the nature of the precursor: nanostructured copper phosphate forms from (III), (IV) and (V) and CuO from (I), (II), (VI) and (VII). The morphologies of the products are also strongly affected by the nature of the precursor; for instance, $Cu_2P_2O_7$ obtained from (IV) and (V) shows a range or surface deposited crystals ranging from 50 -100 nm in size and from (V), single crystal dots form with an areal density of 5.1 – 7.7 Gigadots/in^2. CuO obtained from (VI) and (VII) precursors has either a dense or foam-like morphology, respectively. The use of chitosan polymer as a solid-state template/stabilizer induces the formation of CuO nanoparticles. The morphology of CuO deposited on Si from pyrolysis of (VI) depends on the polymer/Cu meta ratio. Nanostructure size was also affected by the molar ratio of the (polymer)$(CuCl_2)_n$ type precursors; the smallest nanoparticles are obtained from the lowest Cu(II)/polymer ratio. Low temperature magnetic measurements on the CuO nanocrystals suggest superparamagnetic behavior. The results suggest a method of compositional, shape and morphological control of the nanostructures through the structure of the precursors.

Acknowledgements Financial support by FONDECYT (project 1085011) is gratefully acknowledged. Part of this work was conducted under the framework of the INSPIRE programme, funded by the Irish Government's Programme for Research in Third Level Institutions, Cycle 4, National Development Plan 2007-2013.

References

1. A. S. Edelstein, R. C. Cammarata (ed), *Nanomaterials: Synthesis Properties and Applications.* J. W. Arrowsmith Ltd, Bristol (2000).

2. K. J. Klabunde, in *Nanoscale Materials in Chemistry*, Wiley Interscience, New York (2001).

3. C. N. Rao, A. Muller and A. K. Cheetham (ed), *The Chemistry of Nanomaterials*, Synthesis, Properties and Applications. Wiley-VCH, Weinheim, vol. 2, pp. 170-207 (2004).

4. a) S. Anadan, J. Yang, *Experimental Nanoscience* **2**, 23 (2002). b) Ch. Kuo, M. H. Huang, *Nano Today* **5**, 106 (2010).

5. For a discussion of solid–state method of prepare nanoparticles see: C. Diaz and M.L. Valenzuela in "Metallic Nanostructures Using Oligo and Polyphosphazenes as Template or Stabilizer in Solid State" in Encyclopedia of Nanoscience and Nanotechnology, H.S Nalwa Ed., American Scientific Publishers (2009) in press.

6. N. Kawahashi and H. Shiho, *J. Mater. Chem.* **10**, 2294 (2000).

7. J. F. Xu, W. Ji, Z. X. Shen, S. H. Tang, X. R. Ye, D. Z. Jia, X. Q. Xin, *J. Solid State. Chem.* **147**, 516 (1999).

8. T. Yu, X. Zhao, Z. X. Shen, Y. H. Wu, W. H. Su, *J. Cryst. Growth* **268**, 590 (2004).

9. L.-I. Hung, Ch.-K. Tsung, W. Huang, P. Yang, *Adv. Mater.* **22**, 1 (2010).

10. L. Wang, J. Luo, M. Schadt , Ch-Jian Zhong, *Langmuir* **26**, 618 (2010).

11. L.S. Huang, S. G. Yang, T. Li, B. X. Gu, Y. W. Du, Y. N. Lu, S. Z. Shi, *J. Cryst. Growth* **260**, 130 (2004).

12. X. Jiang, T. Herricks and Y. Xia, *Nano Lett.* **2**, 1333 (2002).

13. Z. Yang, J. Xu, W. Zhang, A. Liu and Sh. Tang, *J. Solid State Chem.* **180**, 1390 (2007).

14. J. Morales, L. Sanchez, F. Martin, J. R. Ramo-Barrado, M. Sanchez, *Thin Solid Films* **474**, 133 (2005).

15. A.-M. Cao, J. D. Monnel, Ch. Matranga, J.-M. Wu, L.-L. Cao D. Gao, *J. Phys. Chem. C*, **111**, 18624 (2007).

16. Y. Xing, Z. Liu and S. L. Suib, *Chem. Mater.* **19**, 4820 (2007).

17. X. Wu, G. Shi, S. Wang and P. Wu, *Eur. J. Inorg. Chem.* 4775 (2005).

18. R. Liu, D. Zhao, *Chemosphere* **68**, 1867 (2007).

19. C. Díaz, M. L. Valenzuela, L. Zuñiga, C. O'Dwyer, *J. Inorg. Organomet. Polym.* **19**, 507 (2009).

20. J. Jimenez, A. Laguna, M. Benouazzane, J. A. Sanz, C. Díaz, M. L. Valenzuela, P. G. Jones, *Chem. Eur. J*. **15**, 13509 (2009).

21. C. Diaz, M. L. Valenzuela**,** D. Bravo, V. Lavayen and C. O'Dwyer, *Inorg. Chem*. **47,** 11561 (2008).

22. C. Díaz and M. L. Valenzuela, *Macromolecules* **39**, 103 (2006).

23. C. Díaz, P. Castillo and M. L. Valenzuela, *J. Cluster Sci.* **16**, 515 (2005).

24. C. Díaz and M. L. Valenzuela, *J. Inorg. Organomet. Polym.* **16**, 123 (2006).

25. C. Díaz and M. L. Valenzuela, *J. Inorg. Organomet. Polym.* **16**, 419 (2006).

26. C. Díaz, M. L. Valenzuela, S. Ushak, V. Lavayen and C. O'Dwyer, *J. Nanosci. Nanotechnol.* **9**, 1825 (2009).

27. K. Desai, K. Kit, J. Jiajie, S. Zivanovic, *Biomacromolecules* **9**, 1000 (2008).

28. J. Brugnerotto, J. Lizardi, F.M. Goycoolea, W.Arguelles-Monal, J. Desbrieres, M. Rinaudo, *Polymer* **42**, 3569 (2001).

29. H. Huang X. Yang, *Carbohydrate Research* **339**, 2627 (2004).

30. M. Adlim, M.A. Bakar, K. Kong Live and J. Ismail, *J. Mol. Cat.* **212**, 141 (2004).

31. K. Okitsu, Y. Mizukoshi, T. A. Yamamoto, Y. Maeda and Y. Nagata, *Mater. Lett.* **61**, 3429 (2007).

32. P. Guo, W. Wenyan, G.Liang, P. Yao, *J. Colloid. Interf. Sci.* **323**, 229 (2008).

33. L. A. Belfiore, M. P. Curdie, E. Ueda, *Macromolecules* **26**, 6908 (1993).

34. A. Haynes, P. M. Maitlis, R. Quyoum, C. Pulling, H. Adams, S. E. Spey, R.W. Strange. *J. Chem. Soc. Dalton Trans,* 2565 (2002).

35. C. V. Franco, M. M. da SilvaPaula, G. Goulart, L. F. De Lima, L. K. Noda, N. S. Goncalves, *Mater. Letters* **60**, 2549 (2006).

36. F. Wen, W. Zhang, G. Wei, Y. Wang, J. Zhang, M. Zhang, L. Shi, *Chem. Mater.* **20**, 2144 (2008).

37. S. Klingelfer, W. Heitz, A. Greiner, S. Oestreich, S. Forster, M. Antoinietti, *J. Am. Chem. Soc.* **119**, 10116 (1997).

38. P. Zheng , X. Jiang, X. Zhang, L. Shi, *Langmuir* **22**, 9393 (2006).

39. H. Zou, Sh. Wu, J. Shen, *Langmuir* **24**, 10453 (2008).

40. M. R. Churchill and K.L. Kalra, *Inorg. Chem.* **13**, 1065 (1974).

41. C. Diaz and M. L. Valenzuela, *Polyhedron* **21**, 909 (2002).

42. (a) C. Diaz, M. L. Valenzuela, A. Laguna, V. Lavayen, J. Jimenez, L. Power and C. O'Dwyer, *Langmuir* **26**, 10223 (2010) ; (b) C. Diaz, V. Lavayen, C. O'Dwyer, *J. Solid-State Chem.* **183**, 1595 (2010).

43. B. D. Cullity. Elements of X-ray Diffraction, 2nd Edition, Addison-Wesley, Reading, MA, (1978).

44. X. K. Chen, J. C. Irwin, J. P. Franck, *Phys. Rev. B* **52**, R13130 (1995).

45. Y. W. Zhu, A. M. Moo, T. Yu, X. J. Xu, X. Y. Gao, Y. J. Liu, C. T. Lim, Z. X. Shen, C. K. Ong, A. T. S. Wee, J. T. L. Thong, C.H. Sow, *Chem. Phys. Lett.* **419**, 458 (2006).

46. A. Kudelski, B. Pettinger *Surf. Sci.* **566–568**, 1007 (2004).

47. W.T. Yao, S.H. Yu, Y. Zhou, J. Jiang, Q. Song Wu, L. Zhang, J. Jiang, *J. Phys. Chem. B* **109**, 14011 (2005).

48. A. C. Ferrari, J. Robertson, *Phys. Rev. B.* **61**, 14095 (2000).

49. M. Kilo, C. Schild, A. Wokaun, A. Baiker, *J. Chem. Soc. Faraday Trans.* **88**, 1453 (1992)

50. M. Kaur, K. P. Muthe, S. K. Despande, S. Choudhury, J. B. Singh, N. Verma, S. K. Gupta, J. V. Yakhmi *J. Cryst. Growth* **289**, 670 (2006).

51. Y. W. Zhu, A. M. Moo, T. Yu, X. J. Xu, X. Y. Gao, Y. J. Liu, C. T. Lim, Z. X. Shen, C. K. Ong, A. T. S. Wee, J. T. L. Thong and C. H. Sow, *Chem. Phys. Lett.* **419**, 458 (2006).

52. G. N. Rao, Y. D.Yao and J. W. Chen, *J. Appl. Phys.***105**, 93901 (2009).

53. T. I. Arbuzava, B. A. Gizhevskii, S.V. Naumov, A. V. Korolev, V. L. Arbuzov, K. V. Shanov and A. P. Druzhkov, *J. Magn. Magn. Mater*. **258**, 342 (2003).

54. A. Punnnose, M. S. Seehra, *J. Appl. Phys*. **91,** 7766 (2002).

55. A. Punnnose, H. Magnone, M.S. Seehra, *Phys. Rev. B,* **64**, 174420 (2002).